

# Generalizable Neural Electromagnetic Inverse Scattering

Yizhe Cheng\* Chunxun Tian\* Haoru Wang Wentao Zhu Xiaoxuan Ma Yizhou Wang

Peking University

{ez\_cheng, tianchunxun, ou524u}@stu.pku.edu.cn

{wtzhu, maxiaoxuan, yizhou.wang}@pku.edu.cn

Project page: <https://gomenei.github.io/GenEISP/>

## Abstract

Solving Electromagnetic Inverse Scattering Problems (EISP) is fundamental in applications such as medical imaging, where the goal is to reconstruct the relative permittivity from scattered electromagnetic field. This inverse process is inherently ill-posed and highly nonlinear, making it particularly challenging. A recent machine learning-based approach, Img-Interiors, shows promising results by leveraging continuous implicit functions. However, it requires case-specific optimization, lacks generalization to unseen data, and fails under sparse transmitter setups (*e.g.*, with only one transmitter). To address these limitations, we revisit EISP from a physics-informed perspective, reformulating it as a two-stage inverse transmission–scattering process. This formulation reveals the induced current as a generalizable intermediate representation, effectively decoupling the nonlinear scattering process from the ill-posed inverse problem. Built on this insight, we propose the *first generalizable physics-driven* framework for EISP, comprising a current estimator and a permittivity solver, working in an *end-to-end* manner. The current estimator explicitly learns the induced current as a physical bridge between the incident and scattered field, while the permittivity solver computes the relative permittivity directly from the estimated induced current. This design enables data-driven training and generalizable *feed-forward* prediction of relative permittivity on unseen data while maintaining strong robustness to transmitter sparsity. Extensive experiments show that our method outperforms state-of-the-art approaches in reconstruction accuracy, generalization, and robustness. Notably, it achieves high-quality results even with a single transmitter—a setting where prior methods consistently fail. This work offers a fundamentally new perspective on electromagnetic inverse scattering and represents a major step toward cost-effective practical solutions for electromagnetic imaging.

## 1 Introduction

Electromagnetic waves can penetrate object surfaces, making them essential for non-invasive imaging [14, 26]. At the core of electromagnetic imaging lies the Electromagnetic Inverse Scattering Problems (EISP), which seeks to reconstruct an object’s relative permittivity from measured scattered electromagnetic field [24, 5]. By solving EISP, we can accurately recover internal structures without physical intrusion [33], enabling a range of scientific and industrial applications, such as safer and more cost-effective alternatives to X-rays and MRI scans [3, 26, 24].

\*Equal contribution, random order.

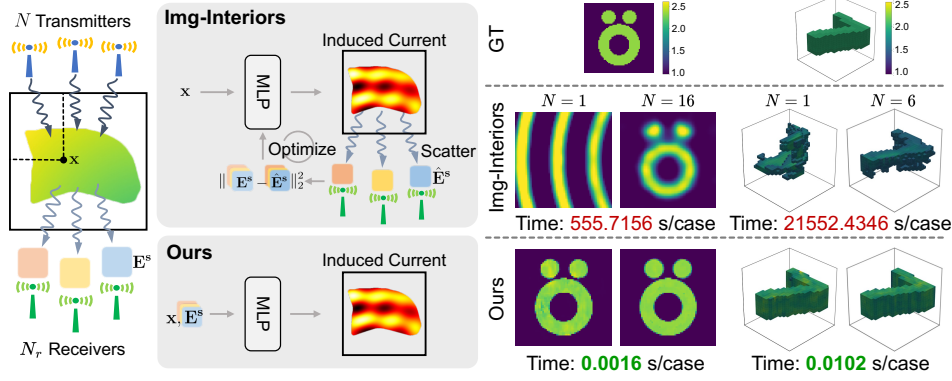


Figure 1: **Comparison between our method and the previous state-of-the-art.** **Left:** Img-Interiors [22] requires case-specific optimization to reconstruct the permittivity and lacks generalization capability. In contrast, our method is the *first generalizable physics-driven* framework that operates in an *end-to-end, feed-forward* manner for solving inverse scattering. By modeling the induced current as a generalizable intermediate representation, our method decouples the nonlinear scattering process from the ill-posed inversion (Sec. 3), enabling data-driven training with strong generalization. **Right:** Our method yields more accurate reconstructions than Img-Interiors [22] on unseen cases. It remains robust even with a *single* transmitter and achieves real-time inference with over  $300,000\times$  speed-up.

However, EISP is inherently highly nonlinear and ill-posed, making accurate and efficient reconstruction a significant challenge [27, 5, 18, 46]. Recent machine learning-based approaches [34, 21, 39], such as PGAN [34] and PhysicsNet [21], typically begin with an initial solution derived from traditional numerical methods [2, 44, 4] such as BP [2] and treat the task as image-to-image translation. However, this overlooks the underlying scattering physics, leading to suboptimal results [21, 40, 39, 22]. To address this, more recent work, Img-Interiors [22], integrates scattering mechanisms into the network architecture. Nevertheless, this approach requires case-by-case optimization, which is time-consuming and prone to local minima, resulting in reconstruction failures (see Fig. 1). Moreover, existing methods heavily rely on dense transmitter arrays, which are typically impractical—and sometimes even infeasible—in real-world applications due to hardware cost, power consumption, and system complexity. In certain scenarios such as ground-penetrating radar, through-wall imaging, and medical imaging, spatial or safety constraints may restrict signal transmission to a single direction or a limited area. Therefore, it is highly desirable for reconstruction methods to perform well under sparse-transmitter settings. However, due to the inherent ill-posedness and increased difficulty of the problem, this setting remains relatively underexplored in the literature.

To address these limitations, we revisit the physical model of EISP and reformulate it as a two-stage inverse transmission–scattering process, where the induced current naturally emerges as a transmitter-agnostic and generalizable intermediate representation. The induced current not only bridges the two stages but also exhibits clear physical interpretability and favorable mathematical properties. This formulation effectively decouples the nonlinear scattering from the ill-posed inverse problem, enabling us to learn inverse scattering through a data-driven way. Based on this insight, we

propose the **first generalizable, physics-driven** framework that operates **end-to-end** with two core modules: a *current estimator* and a *permittivity solver*, as illustrated in Fig. 2. The former learns the induced current as a physical intermediary bridging the incident and scattered field, while the latter computes the relative permittivity directly from the estimated current, guided by physics. This design enables data-driven training and fast, **feed-forward** inference, achieving accurate and generalizable predictions on unseen scenarios. See Tab. 1 for a conceptual comparison with existing EISP methods.

Extensive experiments demonstrate that our model outperforms existing State-of-the-Art (SOTA) methods on multiple benchmark datasets. It generalizes well to diverse scenarios and naturally

Table 1: **Comparison of existing EISP methods.**  $\emptyset$  denotes not applicable.

Method	end2end	feed-forward	physics	generalize
BP [2]	$\emptyset$	$\emptyset$	✓	$\emptyset$
2-fold/Gs SOM [44, 4]	✗	✓	✓	✗
BPS, PGAN [39, 34]	✗	✓	✗	✓
Physics-Net [21]	✗	✓	✓	✓
Img-Interiors [22]	✓	✗	✓	✗
<b>Ours</b>	✓	✓	✓	✓

extends to 3D data while maintaining high reconstruction accuracy. Notably, by leveraging the induced current as a physically meaningful intermediate representation, our model remains robust even under the challenging **single-transmitter setting**, where all prior methods fail, which highlights its strong practical potential in real-world applications. In summary, our contributions are three-fold: 1) We propose a fundamentally new perspective by reformulating EISP as a two-stage transmission–scattering process. This decouples the nonlinear scattering from the ill-posed inversion and introduces the induced current as a generalizable, transmitter-agnostic intermediate representation. 2) Based on this formulation and representation, we develop the first *generalizable, physics-driven* framework that operates *end-to-end*, enabling data-driven learning for inverse scattering with strong physical interpretability. 3) Extensive experiments show that our method outperforms existing SOTA approaches, especially under the challenging single-transmitter setting, marking a concrete step toward cost-effective and practical electromagnetic imaging solutions.

## 2 Related Work

### 2.1 Electromagnetic Inverse Scattering Problems (EISP)

Solving EISP is to determine the relative permittivity of the scatterers based on the scattered field measured by the receivers, thereby obtaining internal imaging of the object. The primary challenges of EISP arise from its nonlinearity, ill-posedness, and errors introduced by the discretization [27, 5, 18, 46, 22]. Traditional methods for solving EISP can be categorized into non-iterative [32, 10, 15, 2] and iterative [4, 45, 41, 16, 36] approaches. Non-iterative methods, such as the Born approximation [32], the Eytov approximation [10, 15], and the backpropagation (BP) method [2], solve nonlinear equations through linear approximations, which inevitably lead to poor quality of the results. For better reconstruction quality, iterative methods [44, 4, 45, 41, 16, 36, 11] such as 2-fold Subspace Optimization Method (SOM) [44] and Gs SOM [4] are proposed. To further overcome the ill-posedness of EISP, diverse regularization approaches and prior information have been widely applied [25, 31, 20, 1]. However, all of these methods are not generalizable and can be time-consuming because of the iterative schemes [21].

### 2.2 Machine Learning for EISP

Recent studies shift to leverage neural networks to solve this problem and demonstrate promising results [13, 19]. Some work [39, 18, 43, 42, 30, 34] adopt a two-stage strategy: they use non-iterative methods such as BP [2] to generate initial estimates, which are then refined using image-to-image neural networks. While these approaches offer a degree of generalization, they treat the EISP purely as an image translation task, ignoring the underlying physics and scattering mechanisms. Consequently, they are prone to failure and often produce unreliable results [17, 28], especially when the initialization is ambiguous. Physics-Net [21] attempts to address this by introducing physical supervision during training. However, it is not end-to-end and remains dependent on BP initialization [2], limiting its generalization. When faced with vague initializations, these approaches tend to “hallucinate” outputs rather than solving the problem based on physical principles (see Fig. 4). A more recent approach, Img-Interiors [22], integrates scattering mechanisms into the network architecture and achieves accurate reconstructions. However, it requires case-specific optimization, limiting generalization and making it vulnerable to local minima, often leading to failure in complex or unseen settings (see Figs. 3 and 6). Moreover, it fails under a single transmitter setting. While our method is also learning-based, it is the first feed-forward and physics-driven framework that simultaneously achieves strong generalization and elegantly integrates physical models into the network architecture. As a result, it consistently outperforms SOTA methods, particularly in the challenging single-transmitter setting where prior approaches fail.

## 3 Revisit EISP

We revisit EISP from a *physics-driven* perspective. In the forward process, the transmitters produce incident electromagnetic field  $\mathbf{E}^i$  to the scatterer, generating scattered electromagnetic field  $\mathbf{E}^s$ . EISP is the inverse problem of the forward process. That is, for an unknown scatterer, we apply certain incident field  $\mathbf{E}^i$  to it, and measure the scattered field  $\mathbf{E}^s$  as our input. Our goal is to reconstruct the relative permittivity  $\epsilon_r$  throughout the scatterer. For a detailed background introduction of the physical model of EISP, please refer to our supplementary material (Appx. A).

We discretize the region of interest  $\mathcal{D}$  into  $M \times M$  subunits to express relative permittivity as an  $M \times M$  matrix. Then we flatten it, making relative permittivity  $\epsilon_r$  a vector of length  $M^2$ . Correspondingly, incident field  $\mathbf{E}^i$  and induced current  $\mathbf{J}$  are also discretized and turned into vectors. Rather than treating EISP as a monolithic inverse problem, we reformulate the forward process of EISP as a two-stage transmission–scattering process, as illustrated in Fig. 2.

For the transmission stage, the incident field  $\mathbf{E}^i$  excites the induced current  $\mathbf{J}$ . Using the method of moments [29], the total field  $\mathbf{E}^t$  for a given transmitter can be expressed as [6]:

$$\mathbf{E}^t = \mathbf{E}^i + \mathbf{G}^d \cdot \mathbf{J}, \quad (1)$$

where  $\mathbf{E}^t$  is a vector of length  $M^2$ , and  $\mathbf{G}^d$  is a constant  $M^2 \times M^2$  matrix representing the discrete free-space Green’s function in  $\mathcal{D}$ . The induced current field  $\mathbf{J}$  satisfies:

$$\mathbf{J} = \text{Diag}(\boldsymbol{\xi}) \cdot \mathbf{E}^t, \quad (2)$$

where  $\boldsymbol{\xi} = \epsilon_r - 1$ ,  $\text{Diag}(\boldsymbol{\xi})$  represents a diagonal matrix whose leading diagonal consists of  $\boldsymbol{\xi}$ . Since the rate of  $\mathbf{J}$  and  $\text{Diag}(\boldsymbol{\xi})$  is  $\mathbf{E}^t$  as Eq. (2) indicates, and  $\mathbf{E}^t$  is not a constant because it is in turn influenced by  $\mathbf{J}$  according to Eq. (1), the relationship between  $\mathbf{J}$  and  $\boldsymbol{\xi}$  exhibits nonlinearity, which arises physically from multiple scattering effects [5]. However, as  $\mathbf{E}^i$ ,  $\mathbf{E}^t$ , and  $\mathbf{J}$  share the same dimensions, this stage does not introduce ill-posedness. Thus, once  $\mathbf{J}$  is determined,  $\boldsymbol{\xi}$  can be computed directly, and further,  $\epsilon_r$  can be computed by  $\epsilon_r = \mathbf{J} \cdot (\mathbf{E}^i + \mathbf{G}^d \cdot \mathbf{J})^{-1} + 1$ .

In the scattering stage,  $\mathbf{J}$  serves as a new source to emit  $\mathbf{E}^s$ . For  $N_r$  receivers, the scattered field  $\mathbf{E}^s$  can be got through  $\mathbf{E}^s = \mathbf{G}^s \cdot \mathbf{J}$ , where  $\mathbf{G}^s$  is a constant  $N_r \times M^2$  matrix representing the discrete Green’s function mapping the induced current  $\mathbf{J}$  to the scattered field  $\mathbf{E}^s$ . Since  $N_r \ll M^2$  in practice, reconstructing the induced current  $\mathbf{J}$  from the scattered field  $\mathbf{E}^s$  is ill-posed. However, unlike the transmission stage, this mapping is linear because there is no multiple scattering.

In summary, the transmission stage is a nonlinear but well-posed process, while the scattering stage is a linear yet ill-posed inverse problem. By using  $\mathbf{J}$  to bridge the incident and scattered fields, we effectively decouple nonlinearity and ill-posedness into two distinct stages, offering a novel perspective for EISP problems.

## 4 Method

### 4.1 Overview

As discussed in Sec. 3, we decouple EISP into two physical stages: inverse scattering and inverse transmission, and identify the induced current field  $\mathbf{J}$  as a crucial role in bridging the relative permittivity and the scattered field in EISP. Building on this insight, we design a framework comprising a current estimator and a permittivity solver, as illustrated in Fig. 2. The current estimator solves the inverse scattering problem by utilizing a neural network to learn the mapping from the scattered field  $\mathbf{E}^s$  to the current field  $\mathbf{J}$ . The permittivity solver addresses the inverse transmission problem according to Eq. (5), which can directly compute the relative permittivity  $\epsilon_r$  from the incident field  $\mathbf{E}^i$  and the predicted current field  $\hat{\mathbf{J}}$ . After obtaining the relative permittivity estimates  $\{\hat{\epsilon}_r^{(1)}, \hat{\epsilon}_r^{(2)}, \dots, \hat{\epsilon}_r^{(N)}\}$  for each transmitter, we then fuse the relative permittivity values across all transmitters to produce the final relative permittivity  $\hat{\epsilon}_r$ .

In the following, we detail the intermediate representation  $\mathbf{J}$  (Sec. 4.2), our model architecture (Sec. 4.3), and the training losses (Sec. 4.4).

### 4.2 Intermediate Representation – the Induced Current

We first justify our choice of the induced current  $\mathbf{J}$  as the intermediate representation by highlighting three key mathematical properties: (i) physical additivity, (ii) simplification of the inverse process, and (iii) invariance to the number of transmitters. **Physical Additivity.** As a vector field, the induced current  $\mathbf{J}$  naturally satisfies the principle of linear superposition. This property aligns with the additive behavior commonly exploited in neural network architectures. **Simplification of the Inverse Process.** As revealed in Sec. 3, in the scattering stage, the scattered field  $\mathbf{E}^s$  has an explicit linear relationship with the current field  $\mathbf{J}$ , expressed through the Green’s function  $\mathbf{G}^s$ . This mapping avoids the traditional nonlinear coupling in relative permittivity  $\epsilon_r$  and the scattered field  $\mathbf{E}^s$ . By eliminating inherent nonlinearities, the model can concentrate exclusively on resolving the ill-posed nature of

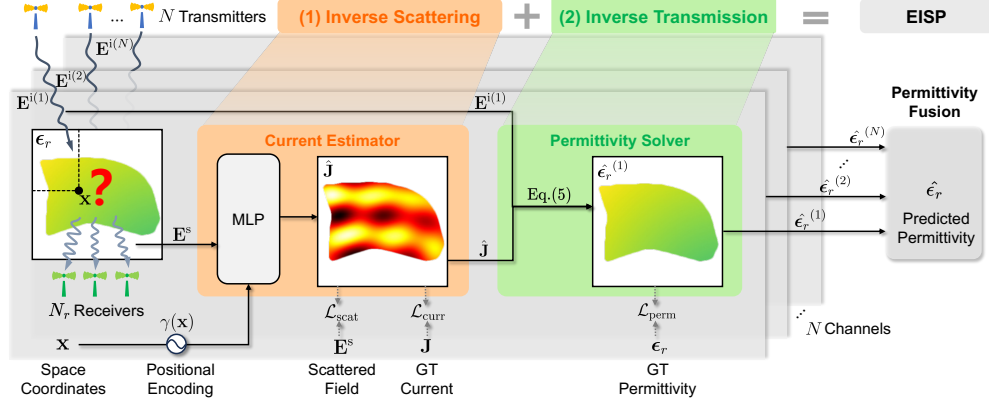


Figure 2: **Overview of our method.** Our pipeline consists of two core modules: (1) a current estimator and (2) a permittivity solver. Given the scattered electromagnetic field  $\mathbf{E}^s$  and a query position  $\mathbf{x}$ , the current estimator predicts the induced current  $\hat{\mathbf{J}}(\mathbf{x})$ . To enhance spatial expressiveness, we apply positional encoding  $\gamma(\mathbf{x})$  to the query position. The permittivity solver then computes the relative permittivity based on the predicted current  $\hat{\mathbf{J}}$  and the incident field  $\mathbf{E}^i$ , following Eq. (5). The final relative permittivity  $\hat{\epsilon}_r$  is obtained by aggregating predictions across all  $N$  transmitters. During training, dashed lines indicate the applied loss terms.

the inverse problem. **Invariance to the Number of Transmitters.** Crucially, the use of current as a scene representation is inherently invariant of the number of transmitters. Even in cases with only a single transmitter, our method remains fully functional. The property ensures strong adaptability to varying measurement configurations.

By leveraging the superposition principle, this physically motivated feature representation reformulates the inverse problem into a computable nonlinear process (transmission stage), coupled with a linear scattering process of the current field, thereby improving tractability and enhancing generalization performance.

### 4.3 Model Architecture

Based on the reformulation in Sec. 3 and our choice of current as an intermediate representation, we design a framework that decouples the problem into two stages, each handled by a dedicated module, as illustrated in Fig. 2. Our framework consists of two core modules: (1) a current estimator and (2) a permittivity solver.

**Current Estimator.** This module addresses the scattering stage described in Sec. 3, which is a linear but ill-posed inverse problem. Conventional analytical methods fail to provide stable solutions due to its ill-posed nature. However, deep neural networks offer a feasible solution: by learning the inverse mapping from the scattered field to the induced current field through training data, the network can generalize this learned mapping to unseen scenarios. Thus, we employ a neural network to learn this ill-posed mapping. Specifically, we adopt a Multilayer Perceptron (MLP) as our network. Our MLP model maps continuous spatial coordinates and the scattered field to their corresponding current values, formulated as:

$$\mathbf{J}_i(\mathbf{x}_i) = F_\theta(\mathbf{E}^s, \gamma(\mathbf{x}_i)), \mathbf{x}_i \in \mathbb{R}^2, \quad (3)$$

where  $\mathbf{x}_i$  is the spatial coordinate,  $\mathbf{E}^s$  is the scattered field measured by all receivers,  $F_\theta(\cdot)$  is an MLP with trainable weights, and  $\mathbf{J}_i$  is the predicted current at the corresponding position. To enhance the model’s fitting capability, we apply positional encoding to the spatial coordinates  $\mathbf{x}_i$ , mapping it into a higher dimensional Fourier feature space. The encoding function is:  $\gamma(\mathbf{x}) = [\sin(\mathbf{x}), \cos(\mathbf{x}), \dots, \sin(2^{\Omega-1}\mathbf{x}), \cos(2^{\Omega-1}\mathbf{x})]$ , where the hyperparameter  $\Omega$  control the spectral bandwidth.

While the MLP outputs pointwise currents, the complete current field  $\hat{\mathbf{J}}$  is reconstructed by sampling the MLP at all grid points  $\{\mathbf{x}_i\}_{i=1}^{M^2}$ :

$$\hat{\mathbf{J}} = \{F_\theta(\mathbf{E}^s, \gamma(\mathbf{x}_i))\}_{i=1}^{M^2}. \quad (4)$$

**Permittivity Solver.** This module addresses the transmission stage described in Sec. 3, where both forward and inverse processes are computationally tractable due to its reversible nature. Given the incident field known from scattering measurements, the relative permittivity and current exhibit a one-to-one mapping despite nonlinear effects. For computing the electric field from the predicted currents, we derive the relative permittivity by jointly solving Eq. (1) and Eq. (2) based on the incident field and the MLP-predicted currents. The inverse equation is given by:

$$\hat{\epsilon}_r = \hat{\mathbf{J}} \cdot (\mathbf{E}^i + \mathbf{G}^d \cdot \hat{\mathbf{J}})^{-1} + 1, \quad (5)$$

where  $\hat{\mathbf{J}}$  is the current field predicted by current estimator,  $\hat{\epsilon}_r$  is the predicted relative permittivity,  $\mathbf{E}^i$  and  $\mathbf{G}^d$  represent the incident electric field and Green’s function, respectively, as introduced in Sec. 3.

Through this process, we obtain the predicted relative permittivity for a single transmitter. However, solving for the current is inherently ill-posed, the predicted current heavily depends on the training distribution of current, which varies significantly across different transmitters. This variation arises because each transmitter’s unique position alters the incident electric field distribution and, consequently, the induced current pattern in the scatterer. To address this, we deploy dedicated current-permittivity solver pairs for each transmitter.

**Permittivity Fusion.** In practice, when we have  $N$  transmitters, we simply aggregate the relative permittivity estimates from all  $N$  transmitters via averaging:  $\hat{\epsilon}_r = \frac{1}{N} \sum_{i=1}^N \hat{\epsilon}_r^{(i)}$ . This multi-transmitter aggregation combines the strengths of each individual solver, achieving a more stable and comprehensive reconstruction.

#### 4.4 Training

Our training objective comprises three loss terms:  $\mathcal{L} = \lambda_{\text{curr}} \mathcal{L}_{\text{curr}} + \lambda_{\text{perm}} \mathcal{L}_{\text{perm}} + \lambda_{\text{scat}} \mathcal{L}_{\text{scat}}$ , where  $\lambda_{\text{curr}}$ ,  $\lambda_{\text{perm}}$ , and  $\lambda_{\text{scat}}$  are hyperparameters that balance the contributions of each term.

The *current* loss  $\mathcal{L}_{\text{curr}} = \|\hat{\mathbf{J}} - \mathbf{J}\|^2$  supervises the predicted current  $\hat{\mathbf{J}}$  against the Ground Truth (GT) current  $\mathbf{J}$  using the Mean Squared Error (MSE) loss. The *permittivity* loss  $\mathcal{L}_{\text{perm}} = \|\hat{\epsilon}_r - \epsilon_r\|^2$  encourages accurate reconstruction of the relative permittivity  $\epsilon_r$ . The *scattering* loss  $\mathcal{L}_{\text{scat}} = \|\hat{\mathbf{E}}^s - \mathbf{E}^s\|^2$  enforces consistency between the predicted current  $\hat{\mathbf{J}}$  and the GT scattered field  $\mathbf{E}^s$ , where the predicted field is computed as  $\hat{\mathbf{E}}^s = \mathbf{G}^s \cdot \hat{\mathbf{J}}$  according to the scattering stage in Sec. 3.

## 5 Experiments

### 5.1 Setup

**Datasets.** We train and test our model on standard benchmarks used for EISP following previous work. 1) Synthetic Circular-cylinder dataset (Circular) [22] is synthetically generated comprising images of cylinders with random relative radius, number, and location and permittivity. 2) Synthetic MNIST dataset (MNIST) [9] contains grayscale images of handwritten digits. For the two synthetic datasets we add 5% level of noise. 3) Real-world Institut Fresnel’s database (IF) [12] contains three different dielectric scenarios, namely FoamDielExt, FoamDielInt, and FoamTwinDiel. 4) Synthetic 3D MNIST dataset (3D MNIST) [8] contains 3D data of handwritten digits. For more details about datasets, please refer to Appx. B.

**Baselines and Metrics.** We maintain the same settings as in previous studies [39, 34, 30] to ensure a fair comparison. We compare our method with three traditional methods and four deep learning-based approaches: 1) **BP** [2]: A traditional non-iterative inversion algorithm. 2) **2-fold SOM** [44]: A traditional iterative minimization scheme by using SVD decomposition. 3) **Gs SOM** [4]: A traditional subspace-based optimization method by decomposing the operator of Green’s function. 4) **BPS** [39]: A CNN-based image translation method with an initial guess from the BP algorithm. 5) **Physics-Net** [21]: A CNN-based approach that incorporates physical phenomena during training. 6) **PGAN** [34]: A CNN-based approach using a generative adversarial network. 7) **Img-Interiors** [21]: An implicit approach optimized by forward calculation. Following previous work [21], we evaluate the quantitative performance of our method using PSNR [37], SSIM [38], and Relative Root-Mean-Square Error (MSE) [34].

Table 2: **Quantitative comparison results with SOTA methods.** For Circular and MNIST datasets, we report results under two noise levels: 5% and 30%. The best results are shown in **bold**, and the second-best results are underlined.

Method	MNIST (5%)			MNIST (30%)			Circular (5%)			Circular (30%)			IF		
	MSE ↓	SSIM ↑	PSNR ↑	MSE ↓	SSIM ↑	PSNR ↑	MSE ↓	SSIM ↑	PSNR ↑	MSE ↓	SSIM ↑	PSNR ↑	MSE ↓	SSIM ↑	PSNR ↑
Number of Transmitters: $N = 16$															
$N = 8/18$															
BP [2]	0.177	0.719	16.43	0.178	0.716	16.38	0.052	0.905	27.41	0.053	0.904	27.42	0.190	0.779	16.19
2-fold SOM [44]	0.154	0.757	20.93	0.156	0.738	20.84	0.031	0.917	32.23	0.038	0.889	30.63	-	-	-
Gs SOM [4]	<u>0.072</u>	0.923	<u>28.31</u>	<u>0.081</u>	0.901	<b>27.13</b>	<u>0.023</u>	0.946	35.40	<b>0.024</b>	0.937	<b>34.89</b>	0.184	0.790	17.00
BPS [39]	0.093	0.909	25.00	0.105	0.891	23.90	0.027	<u>0.963</u>	33.00	0.029	<b>0.956</b>	32.42	0.310	0.664	17.05
PGAN [34]	0.084	0.916	25.80	0.091	<u>0.910</u>	25.31	0.026	<b>0.966</b>	<u>35.56</u>	0.032	<u>0.947</u>	33.91	<u>0.121</u>	<b>0.926</b>	<u>24.78</u>
Physics-Net [21]	0.075	<u>0.932</u>	26.17	0.093	0.906	24.58	0.027	0.934	32.72	0.030	0.927	32.08	0.170	0.788	18.48
Img-Interiors [22]	0.200	0.863	26.41	0.336	0.760	19.01	0.036	0.947	35.05	0.047	0.932	32.62	0.153	0.837	23.26
<b>Ours</b>	<b>0.055</b>	<b>0.955</b>	<b>29.31</b>	<b>0.077</b>	<b>0.923</b>	<u>26.52</u>	<b>0.021</b>	0.961	<b>36.74</b>	<u>0.027</u>	0.942	<u>34.23</u>	<b>0.119</b>	<u>0.912</u>	<b>24.89</b>
Number of Transmitters: $N = 1$															
BP [2]	0.194	0.698	15.40	0.194	0.696	15.40	0.065	0.892	25.30	0.065	0.892	25.30	0.199	0.770	16.29
2-fold SOM [44]	0.432	0.556	12.49	0.828	0.382	9.45	0.060	0.859	26.63	0.157	0.639	20.07	-	-	-
Gs SOM [4]	0.460	0.598	15.31	0.404	0.557	14.91	0.046	0.888	29.62	0.051	0.862	28.77	0.192	<u>0.779</u>	16.66
BPS [39]	0.189	0.774	18.75	0.205	0.744	17.97	0.045	0.891	29.29	0.055	0.862	27.68	0.348	0.669	16.18
PGAN [34]	<u>0.133</u>	<u>0.867</u>	<u>21.69</u>	0.153	<u>0.830</u>	<u>20.41</u>	<u>0.033</u>	<u>0.932</u>	<u>32.02</u>	<u>0.040</u>	<u>0.914</u>	<u>29.94</u>	0.248	0.680	16.85
PhysicsNet [21]	0.137	0.798	19.98	<u>0.152</u>	0.783	19.38	0.055	0.887	26.60	0.056	0.890	26.48	<u>0.175</u>	0.771	<u>17.45</u>
Img-Interiors [22]	0.422	0.400	13.04	0.701	0.304	9.71	0.204	0.568	17.19	0.330	0.453	12.38	0.305	0.705	17.34
<b>Ours</b>	<b>0.079</b>	<b>0.914</b>	<b>26.41</b>	<b>0.111</b>	<b>0.864</b>	<b>23.56</b>	<b>0.028</b>	<b>0.941</b>	<b>34.16</b>	<b>0.037</b>	<b>0.916</b>	<b>31.93</b>	<b>0.129</b>	<b>0.870</b>	<b>23.94</b>

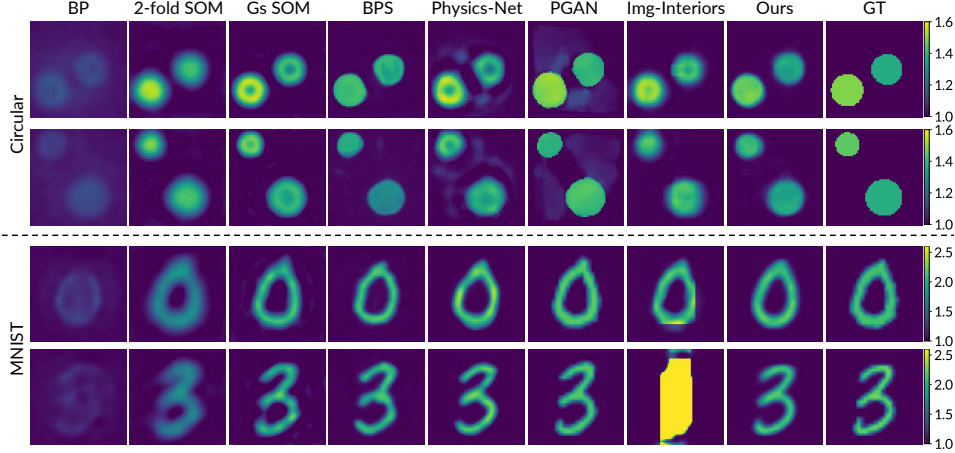


Figure 3: **Qualitative comparison under the multiple-transmitter setting.** The results are obtained with  $N = 16$  transmitters and a noise level of 5%. Colors represent the values of the relative permittivity.

## 5.2 Comparison with SOTAs

### 5.2.1 Multiple Transmitter Evaluation

We begin by comparing our method against prior approaches under the multiple-transmitter setting, using both synthetic and real datasets for comprehensive evaluation. As shown in the upper part of Tab. 2, our method achieves comparable or superior performance to the SOTA in most cases, highlighting the advantages of our decoupled learning scheme and end-to-end training framework across diverse data domains.

In addition, we present a qualitative comparison, as shown in Fig. 3. Traditional methods such as BP[2], Gs SOM [4], and 2-fold SOM [4] are only capable of recovering the coarse shape of the scatterer. BPS [5] produces sharp edges, but the reconstructed shapes are often inaccurate. PGAN [34] achieves accurate shape recovery, yet introduces noticeable background artifacts. Img-Interiors [22] can generate high-quality reconstructions, but occasionally fails due to local optima, as it is based on an iterative optimization process (see the last row). In contrast, our method produces accurate and clean reconstructions across all cases, demonstrating both visual fidelity and robustness.



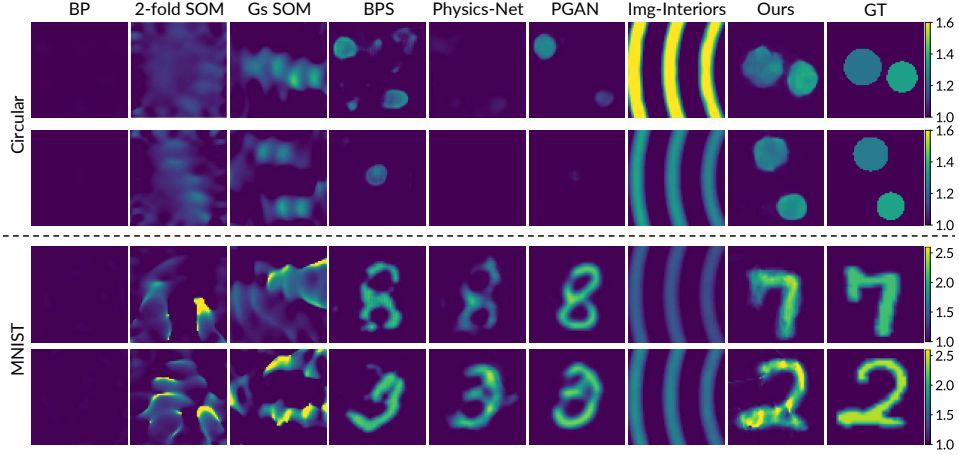


Figure 4: **Qualitative comparison under the single-transmitter setting.** Results are obtained with  $N = 1$  transmitter and noise level of 5%. Colors represent the values of the relative permittivity.

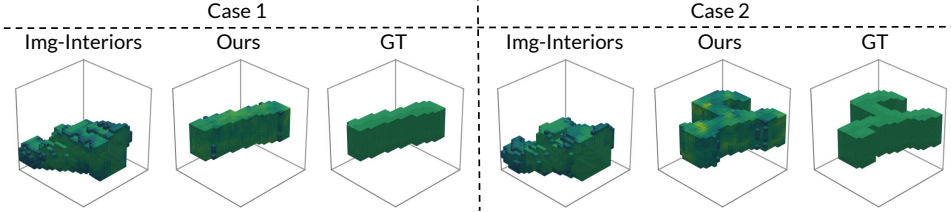


Figure 5: **Qualitative comparison under the single-transmitter setting for 3D reconstruction.** The results are obtained with a single transmitter ( $N = 1$ ). The voxel colors represent the values of the relative permittivity.

### 5.2.2 Single Transmitter Evaluation

Furthermore, we investigate a highly challenging and practically important setting that has been largely underexplored in previous work: performing EISP with a minimal number of transmitters. Specifically, we consider the most extreme case — using only a single transmitter. As shown in the lower part of Tab. 2, our method significantly outperforms all previous approaches across all datasets and noise levels. This highlights the strength of our framework, which uses the induced current as a generalizable and transmitter-agnostic task representation.

To better understand this phenomenon, we present qualitative comparisons in Fig. 4. Traditional methods such as BP[2], Gs SOM [4], and 2-fold SOM [4] produce only blurry reconstructions. Deep learning-based methods like BPS [5], Physics-Net [21], and PGAN [34] tend to “hallucinate” the digit, resulting in wrong shape on the MNIST dataset. Img-Interiors [22] suffers from degeneration and can only reconstruct spherical wave patterns. Among all the methods, only ours can still produce reasonably accurate reconstructions of the relative permittivity under such an extreme condition.

Additionally, our method can be naturally extended to 3D scenarios. Specifically, we predict the induced current along all three spatial directions within a 3D region of interest. Following Img-Interiors [22], we evaluate both methods on the 3D MNIST dataset, and the visual comparison is shown in Fig. 5. It can be observed that our method is able to approximately reconstruct the relative permittivity under this challenging setting, whereas Img-Interiors fails to do so. We also present a comparison of reconstruction quality and runtime for  $N = 6$  in Fig. 1.

### 5.3 Ablation Study

**Noise Robustness.** To simulate real-world sensor noise and related perturbations, we evaluate the robustness of the models by adding noise to the scattered field. Specifically, we consider two levels of noise: a moderate noise level (5%) and a high noise level (30%), and use the resulting scattered fields to reconstruct the scatterers. The quantitative results are presented in Tab. 2. To further illustrate the impact of high noise, we provide qualitative comparisons in Fig. 6. It can be observed that most



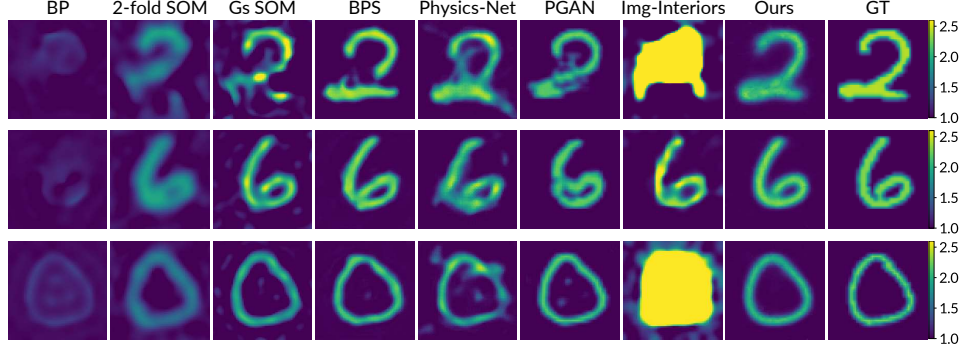


Figure 6: **Qualitative comparison under high noise setting.** The results are obtained with  $N = 16$  transmitters and a noise level of 30%. Colors represent the values of the relative permittivity.

Table 3: **Ablation study on number of transmitters.** Noise levels (5% and 30%) are indicated in parentheses. As transmitter number  $N$  rises, reconstruction metrics improve with diminishing gains.

$N$	MNIST (5%)			MNIST (30%)			Circular (5%)			Circular (30%)		
	MSE ↓	SSIM ↑	PSNR ↑	MSE ↓	SSIM ↑	PSNR ↑	MSE ↓	SSIM ↑	PSNR ↑	MSE ↓	SSIM ↑	PSNR ↑
1	0.079	0.914	26.41	0.111	0.864	23.56	0.028	0.941	34.16	0.037	0.916	31.93
4	0.059	0.947	28.52	0.083	0.910	25.87	0.022	0.956	36.27	0.029	0.935	33.72
8	0.056	0.953	29.06	0.079	0.918	26.23	0.021	0.959	36.60	0.027	0.939	34.07
12	0.054	0.955	29.30	0.077	0.922	26.47	0.021	0.960	36.69	0.027	0.941	34.19
16	0.055	0.955	29.31	0.077	0.923	26.52	0.021	0.961	36.74	0.027	0.942	34.23

baseline methods exhibit noticeable artifacts or even complete failure under severe noise, whereas our method remains robust and is able to preserve the essential structure of the target.

**Transmitter Robustness.** We also investigate the impact of the number of transmitters on reconstruction quality. The corresponding results are presented in Tab. 3. The results demonstrate that our method remains relatively robust even in sparse-transmitter settings. For example, when using  $N = 4$  or  $N = 8$  transmitters, the reconstruction quality degrades only slightly compared to the full setting with  $N = 16$ . This indicates that our approach is well-suited for practical applications, offering greater flexibility and lower deployment costs by reducing reliance on dense transmitter arrays.

**Loss Ablation.** To validate the effectiveness of our proposed loss functions, we conduct ablation studies on both MNIST and IF dataset. As demonstrated in Tab. 4, the introduction of the permittivity loss improves metrics across both experiments. Conversely, the scattering loss alone fails to improve performance and even degrades metrics, as noise introduced during training causes deviations from inverse scattering stage, especially with 30% noise contamination. However, the full model combining both losses achieves optimal results.

Table 4: **Ablation study on loss functions.** Results are obtained with transmitter number  $N = 1$ .

Loss	MNIST (5%)			MNIST (30%)			IF Case 1			IF Case 2		
	MSE ↓	SSIM ↑	PSNR ↑	MSE ↓	SSIM ↑	PSNR ↑	MSE ↓	SSIM ↑	PSNR ↑	MSE ↓	SSIM ↑	PSNR ↑
(a) $\mathcal{L}_{\text{curr}}$	0.082	0.909	25.91	0.115	0.860	23.10	0.156	0.809	20.90	0.118	0.866	23.05
(b) $\mathcal{L}_{\text{curr}} + \mathcal{L}_{\text{perm}}$	0.080	0.914	26.30	0.112	<b>0.867</b>	23.45	0.149	0.847	23.06	0.132	0.843	23.70
(c) $\mathcal{L}_{\text{curr}} + \mathcal{L}_{\text{scat}}$	0.083	0.906	25.96	0.120	0.839	22.91	0.164	0.801	21.14	0.120	0.836	23.66
(d) <b>Ours</b>	<b>0.079</b>	<b>0.914</b>	<b>26.41</b>	<b>0.111</b>	0.864	<b>23.56</b>	<b>0.107</b>	<b>0.897</b>	<b>25.16</b>	<b>0.099</b>	<b>0.896</b>	<b>25.98</b>

## 6 Conclusion

In this work, we propose a generalizable, physics-driven framework for electromagnetic inverse scattering by introducing the induced current as an intermediate representation. This design enables fast, feed-forward reconstruction with strong generalization and robustness, even under sparse transmitter settings. Our results demonstrate the effectiveness and practicality of combining physical modeling with data-driven learning.

**Limitations.** While our method effectively handles sparse transmitter settings, it does not explicitly explore the impact of transmitter placement, which remains an important direction for future work.

## References

- [1] Nicola Anselmi, Lorenzo Poli, Giacomo Oliveri, and Andrea Massa. Iterative multiresolution Bayesian CS for microwave imaging. *IEEE Trans. Antennas Propag.*, 66(7):3665–3677, 2018.
- [2] Kamal Belkebir, Patrick C Chaumet, and Anne Sentenac. Superresolution in total internal reflection tomography. *Journal of the Optical Society of America A*, 2005.
- [3] Martina Teresa Bevacqua, Simona Di Meo, Lorenzo Crocco, Tommaso Isernia, and Marco Pasian. Millimeter-waves breast cancer imaging via inverse scattering techniques. *IEEE Journal of Electromagnetics, RF and Microwaves in Medicine and Biology*, 5:246–253, 2021.
- [4] Xudong Chen. Subspace-based optimization method for solving inverse-scattering problems. *IEEE Transactions on Geoscience and Remote Sensing*, 2009.
- [5] Xudong Chen. *Computational methods for electromagnetic inverse scattering*. John Wiley & Sons, 2018.
- [6] David Colton and Rainer Kress. *Integral Equation Methods in Scattering Theory*. SIAM, 2013.
- [7] David L Colton, Rainer Kress, and Rainer Kress. *Inverse Acoustic and Electromagnetic Scattering Theory*. Springer, 1998.
- [8] David de la Iglesia Castro. 3D mnist: A 3D version of the mnist database of handwritten digits. <https://www.kaggle.com/datasets/daavoo/3d-mnist>.
- [9] Li Deng. The mnist database of handwritten digit images for machine learning research. *IEEE Signal Processing Magazine*, 29(6):141–142, 2012.
- [10] AJ Devaney. Inverse-scattering theory within the rytov approximation. *Optics Letters*, 1981.
- [11] Fuqiang Gao, Barry D Van Veen, and Susan C Hagness. Sensitivity of the distorted born iterative method to the initial guess in microwave breast imaging. *IEEE Transactions on Antennas and Propagation*, 2015.
- [12] Jean-Michel Geffrin, Pierre Sabouroux, and Christelle Eyraud. Free space experimental scattering database continuation: experimental set-up and measurement precision. *Inverse Problems*, 21(6):S117–S130, 2005.
- [13] Ruixu Geng, Yang Hu, Yan Chen, et al. Recent advances on non-line-of-sight imaging: Conventional physical models, deep learning, and new scenes. *APSIPA Transactions on Signal and Information Processing*, 2021.
- [14] Ruixu Geng, Yadong Li, Dongheng Zhang, Jincheng Wu, Yating Gao, Yang Hu, and Yan Chen. Dream-pcd: Deep reconstruction and enhancement of mmwave radar pointcloud. *IEEE Transactions on Image Processing*, 2024.
- [15] Tarek M Habashy, Ross W Groom, and Brian R Spies. Beyond the born and rytov approximations: A nonlinear approach to electromagnetic scattering. *Journal of Geophysical Research: Solid Earth*, 1993.
- [16] Tarek M Habashy, Michael L Oristaglio, and Adrianus T de Hoop. Simultaneous nonlinear reconstruction of two-dimensional permittivity and conductivity. *Radio Science*, 1994.
- [17] Jiate Li, Meng Pang, Yun Dong, Jinyuan Jia, and Binghui Wang. Graph neural network explanations are fragile. In *International Conference on Machine Learning*, 2024.
- [18] Lianlin Li, Long Gang Wang, Fernando L. Teixeira, Che Liu, Arye Nehorai, and Tie Jun Cui. Deepnis: Deep neural network for nonlinear electromagnetic inverse scattering. *IEEE Transactions on Antennas and Propagation*, 67(3):1819–1825, 2019.
- [19] Yadong Li, Dongheng Zhang, Ruixu Geng, Jincheng Wu, Yang Hu, Qibin Sun, and Yan Chen. Ifnet: Imaging and focusing network for handheld mmwave devices. In *IEEE International Conference on Acoustics, Speech and Signal Processing (ICASSP)*, 2024.
- [20] Zicheng Liu, Dominique Lesselier, and Yu Zhong. Electromagnetic imaging of damages in fibered layered laminates via equivalence theory. *IEEE Trans. Comput. Imaging*, 4(2):219–227, 2018.
- [21] Zicheng Liu, Mayank Roy, Dilip K Prasad, and Krishna Agarwal. Physics-guided loss functions improve deep learning performance in inverse scattering. *IEEE Transactions on Computational Imaging*, 2022.
- [22] Ziyuan Luo, Boxin Shi, Haoliang Li, and Renjie Wan. Imaging interiors: An implicit solution to electromagnetic inverse scattering problems. In *ECCV*, 2024.

- [23] Sanjit K Mitra. *Digital signal processing: a computer-based approach*. McGraw-Hill Higher Education, 2001.
- [24] Natalia K. Nikolova. Microwave imaging for breast cancer. *IEEE Microwave Magazine*, 12(7):78–94, 2011.
- [25] Giacomo Oliveri, Marco Salucci, Nicola Anselmi, and Andrea Massa. Compressive sensing as applied to inverse problems for imaging: Theory, applications, current trends, and open challenges. *IEEE Antennas Propag. Mag.*, 59(5):34–46, 2017.
- [26] Declan O’Loughlin, Martin O’Halloran, Brian M Moloney, Martin Glavin, Edward Jones, and M Adnan Elahi. Microwave breast imaging: Clinical advances and remaining challenges. *IEEE Transactions on Biomedical Engineering*, 65(11):2580–2590, 2018.
- [27] Li Pan, Yu Zhong, Xudong Chen, and Swee Ping Yeo. Subspace-based optimization method for inverse scattering problems utilizing phaseless data. *IEEE Transactions on Geoscience and Remote Sensing*, 49(3): 981–987, 2011.
- [28] Meng Pang, Binghui Wang, Mang Ye, Yiu-Ming Cheung, Yintao Zhou, Wei Huang, and Bihan Wen. Heterogeneous prototype learning from contaminated faces across domains via disentangling latent factors. *IEEE Transactions on Neural Networks and Learning Systems*, 2024.
- [29] Andrew F Peterson, Scott L Ray, and Raj Mittra. *Computational methods for electromagnetics*. IEEE Press New York, 1998.
- [30] Yash Sanghvi, Yaswanth Kalepu, and Uday K Khankhoje. Embedding deep learning in inverse scattering problems. *IEEE Transactions on Computational Imaging*, 2019.
- [31] Fangfang Shen, Guanghui Zhao, Zicheng Liu, Guangming Shi, and Jie Lin. SAR imaging with structural sparse representation. *IEEE J. Sel. Topics Appl. Earth Observ. Remote Sens.*, 8(8):3902–3910, 2014.
- [32] M. Slaney, A.C. Kak, and L.E. Larsen. Limitations of imaging with first-order diffraction tomography. *IEEE Transactions on Microwave Theory and Techniques*, 1984.
- [33] Lin-Ping Song, Chun Yu, and Qing Huo Liu. Through-wall imaging (twi) by radar: 2-d tomographic results and analyses. *IEEE Trans. Geosci. Remote. Sens.*, 43:2793–2798, 2005.
- [34] Rencheng Song, Youyou Huang, Kuiwen Xu, Xiuzhu Ye, Chang Li, and Xun Chen. Electromagnetic inverse scattering with perceptual generative adversarial networks. *IEEE Transactions on Computational Imaging*, 2021.
- [35] Allen Taflov, Susan C Hagness, and Melinda Piket-May. Computational electromagnetics: the finite-difference time-domain method. *The Electrical Engineering Handbook*, 2005.
- [36] Peter M van den Berg, AL Van Broekhoven, and Aria Abubakar. Extended contrast source inversion. *Inverse problems*, 1999.
- [37] Zhou Wang and Alan C. Bovik. Mean squared error: Love it or leave it? a new look at signal fidelity measures. *IEEE Signal Processing Magazine*, 26(1):98–117, 2009.
- [38] Zhou Wang, A.C. Bovik, H.R. Sheikh, and E.P. Simoncelli. Image quality assessment: from error visibility to structural similarity. *IEEE TIP*, 13(4):600–612, 2004.
- [39] Zhun Wei and Xudong Chen. Deep-learning schemes for full-wave nonlinear inverse scattering problems. *IEEE Transactions on Geoscience and Remote Sensing*, 57(4):1849–1860, 2019.
- [40] Zhun Wei and Xudong Chen. Physics-inspired convolutional neural network for solving full-wave inverse scattering problems. *IEEE Transactions on Antennas and Propagation*, 67(9):6138–6148, 2019.
- [41] Kuiwen Xu, Yu Zhong, and Gaofeng Wang. A hybrid regularization technique for solving highly nonlinear inverse scattering problems. *IEEE Transactions on Microwave Theory and Techniques*, 2017.
- [42] Kuiwen Xu, Chen Zhang, Xiuzhu Ye, and Rencheng Song. Fast full-wave electromagnetic inverse scattering based on scalable cascaded convolutional neural networks. *IEEE Transactions on Geoscience and Remote Sensing*, 2021.
- [43] Lu Zhang, Kuiwen Xu, Rencheng Song, Xiuzhu Ye, Gaofeng Wang, and Xudong Chen. Learning-based quantitative microwave imaging with a hybrid input scheme. *IEEE Sensors Journal*, 2020.

- [44] Yu Zhong and Xudong Chen. Twofold subspace-based optimization method for solving inverse scattering problems. *Inverse Problems*, 2009.
- [45] Yu Zhong and Xudong Chen. An fft twofold subspace-based optimization method for solving electromagnetic inverse scattering problems. *IEEE Transactions on Antennas and Propagation*, 2011.
- [46] Yu Zhong, Marc Lambert, Dominique Lesselier, and Xudong Chen. A new integral equation method to solve highly nonlinear inverse scattering problems. *IEEE Transactions on Antennas and Propagation*, 64(5):1788–1799, 2016.
- [47] Huilin Zhou, Yang Cheng, Huimin Zheng, Qiegen Liu, and Yuhao Wang. Deep unfolding contrast source inversion for strong scatterers via generative adversarial mechanism. *IEEE Transactions on Microwave Theory and Techniques*, 2022.

This supplementary material provides additional details and results, including the physical model of Electromagnetic Inverse Scattering Problems (EISP) (Appx. A), the experimental setup (Appx. B), and extended experimental results (Appx. C).

## A Physical Model of EISP

The research subject of EISP is scatterers. We can describe scatterers with their relative permittivity  $\epsilon_r(\mathbf{x})$ . The relative permittivity is a physical quantity determined by the material, and it represents the ability to interact with the electromagnetic field of the material. The relative permittivity of vacuum is 1 (and the relative permittivity of air is almost 1), while the relative permittivity of scatterers is over 1. The relative permittivity of metal material is positive infinity, so metal can shield against electromagnetic waves. Thus, scatterers are not composed of metal.

In EISP, the scatterer is placed within the region of interest  $\mathcal{D}$ . The transmitters are placed around  $\mathcal{D}$ , emitting incident electromagnetic field  $E^i$ . The incident field then interacts with the scatterer, exciting the induced current  $J$ . The induced current can act as secondary radiation sources, emitting scattered field  $E^s$ . In fact, for a point in the scatterer, it cannot distinguish the incident field and the scattered field at this point. So, it interacts with the sum of the incident field and the scattered field, aka the total field  $E^t$ . The total field can be described by Lippmann-Schwinger equation [6] as follows:

$$E^t(\mathbf{x}) = E^i(\mathbf{x}) + k_0^2 \int_{\mathcal{D}} g(\mathbf{x}, \mathbf{x}') J(\mathbf{x}') d\mathbf{x}', \mathbf{x} \in \mathcal{D}, \quad (6)$$

where  $\mathbf{x}$  and  $\mathbf{x}'$  are the spatial coordinates.  $k_0$  is the wavelength of the electromagnetic wave determined by the frequency.  $g(\mathbf{x}, \mathbf{x}')$  is the free space Green's function, which represents the impact of the induced current  $J$  at the point  $\mathbf{x}'$  to the total field at the point  $\mathbf{x}$ .  $\mathbf{x} \in \mathcal{D}$  indicates that the total field is within the region of interest  $\mathcal{D}$ . The relationship between the induced current  $J$  and the total field  $E^t$  can be expressed as follows:

$$J(\mathbf{x}) = \xi(\mathbf{x}) E^t(\mathbf{x}), \quad (7)$$

where  $\xi(\mathbf{x}) = \epsilon_r(\mathbf{x}) - 1$ .

The induced current generates scattered field, and we can measure the scattered field with receivers around the region of interest  $\mathcal{D}$ . The scattered field can be expressed as follows:

$$E^s = k_0^2 \int_{\mathcal{D}} g(\mathbf{x}, \mathbf{x}') J(\mathbf{x}') d\mathbf{x}', \mathbf{x} \in S, \quad (8)$$

where  $\mathbf{x} \in S$  indicates that the scattered field is measured by the receivers at surface  $S$  around  $\mathcal{D}$ .

Since digital analysis only applies to discrete variables [23, 35], we discretize equations Eq. (6), Eq. (7), and Eq. (8). The region of interest  $\mathcal{D}$  is discretized into  $M \times M$  square subunits, and we use the method of moment [29] to obtain the discrete scattered field  $\mathbf{E}^s$ <sup>1</sup>. The discrete version of Eq. (6) is as follows:

$$\mathbf{E}^t = \mathbf{E}^i + \mathbf{G}^d \cdot \mathbf{J}, \quad (9)$$

where  $\mathbf{G}^d$  is the discrete free space Green's function from points in the region of interest to points in the region of interest, which is a matrix of the shape  $M^2 \times M^2$ . The discrete version of Eq. (7) is as follows:

$$\mathbf{J} = \text{Diag}(\boldsymbol{\xi}) \cdot \mathbf{E}^t. \quad (10)$$

And the discrete version of Eq. (8) is as follows:

$$\mathbf{E}^s = \mathbf{G}^s \cdot \mathbf{J}, \quad (11)$$

where  $\mathbf{G}^s$  is the discrete free space Green's function from points in the region of interest to the locations of receivers, which is a matrix of the shape  $N_r \times M^2$ .

---

<sup>1</sup>We use the **bold letters** to represent discrete variables.

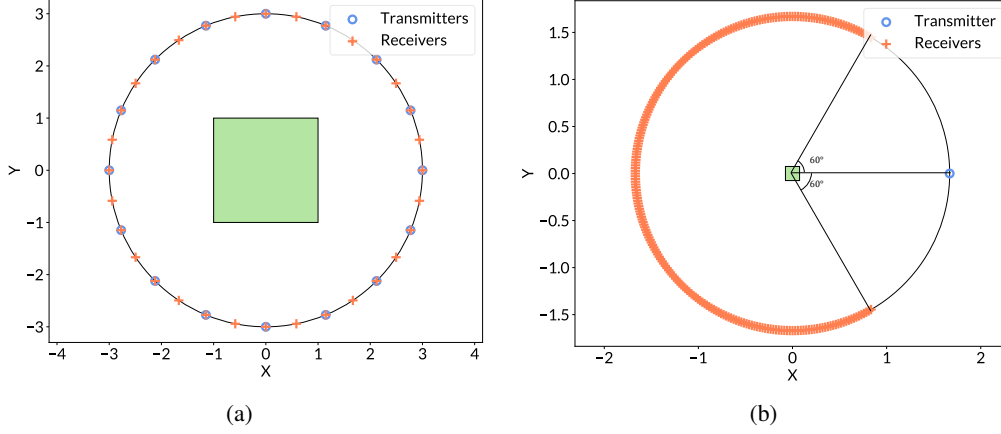


Figure 7: **Positions of transmitters and receivers for 2D data.** (a) For Circular dataset and MNIST dataset, we set up  $N = 16$  transmitters and  $N_r = 32$  receivers. All transmitters and receivers are equally placed. (b) For IF dataset, we set up  $N = 8$  or  $18$  transmitters and  $N_r = 241$  receivers. The transmitters are equally placed (not shown in the figure), and the locations of receivers are determined by the transmitter. For all datasets, the green square represents the region of interest  $\mathcal{D}$ .

## B Details of Experimental Setup

### B.1 Datasets

We strictly follow the established rules in EISP [39, 34, 21] to set the dataset. We train and test our model on standard benchmarks used for EISP.

1) Circular [22] is synthetically generated comprising images of cylinders with random relative radius, number, location, and permittivity between 1 and 1.5.  $60k$  images are generated for training purposes, and  $1.2k$  images for testing.

2) MNIST [9] contains grayscale images of handwritten digits. Similar to previous settings [39, 47], we use them to synthesize scatterers with relative permittivity values between 2 and 2.5 according to their corresponding pixel values. The entire MNIST training set containing  $60k$  images is used for training purposes, while  $1.2k$  images from the MNIST test set are randomly selected for testing.

Following previous work [5, 47] to generate the above two synthetic datasets, we set operating frequency  $f = 400$  MHz. The region of interest is a square with the size of  $2m \times 2m$ . We use 16 transmitters and 32 receivers equally placed on a circle with a radius of  $3m$  ( $N_r = 32$  and  $N = 16$ ). The schematic diagram of the locations of the transmitters and receivers around the region of interest is shown in Fig. 7a. The data are generated numerically using the method of moments [29] with a  $224 \times 224$  grid mesh to avoid inverse crime [7]. To simulate the noise in actual measurement, we add a 5% level of noise to the scattered field  $\mathbf{E}^s$  for regular setting.

3) Real-world IF dataset [12] contains three different dielectric scenarios, namely FoamDielExt, FoamDielInt, and FoamTwinDiel.  $N = 8$  for FoamDielExt and FoamDielInt,  $N = 18$  for FoamTwinDiel, and  $N_r = 241$  for all the cases. The region of interest is a square with the size of  $0.15m \times 0.15m$ . Transmitters and receivers are placed on a circle with a radius of  $1.67m$ . The transmitters are placed equally, and the locations of receivers vary for each transmitter. There is no receiver at any position closer than  $60^\circ$  from the transmitter, and 241 receivers are placed from  $+60^\circ$  to  $+300^\circ$  with a step of  $1^\circ$  from the location of the transmitter. The schematic diagram of the locations of the transmitters and receivers around the region of interest is shown in Fig. 7b. In the real measurement, there is only one transmitter at a fixed location, and the scatterer rotates to simulate the transmitter to be in different directions. There is a movable receiver sequentially measures the scattered field at 241 different locations. After the measurement, the scatterer rotates by a certain angle for next measurement. The angle is  $45^\circ$  for FoamDielExt and FoamDielInt because  $N_r = 8$ , and  $20^\circ$  for FoamTwinDiel because  $N_r = 18$ . As for operating frequency, all cases are measured under many different frequencies, and we take the frequency  $f = 5$  GHz. We evaluate these three

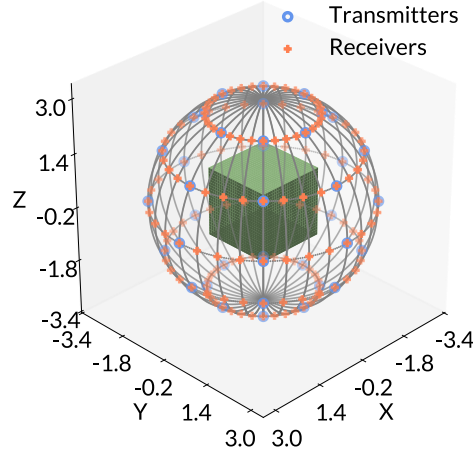


Figure 8: **Positions of transmitters and receivers for 3D MNIST dataset.** There are  $N = 40$  transmitters and  $N_r = 160$  receivers. The green cube represents the region of interest  $\mathcal{D}$ .

scenarios for testing, and use the same settings to synthetically generate 10k images of cylinders with random number and location for training purposes.

4) Synthetic 3D MNIST [8] contains 3D images of handwritten digits. We use them to synthesize scatterers with relative permittivity value of 2.  $N_r = 160$  and  $N = 40$ , and the operating frequency  $f = 400$  MHz. The region of interest is a cube with the size of  $2m \times 2m \times 2m$ . The transmitters and receivers are placed at a sphere with the radius of  $3m$ . For the positions of transmitters, the azimuthal angle ranges from  $0^\circ$  to  $315^\circ$  with the step of  $45^\circ$ , and the polar angle ranges from  $30^\circ$  to  $150^\circ$  with the step of  $30^\circ$ . For the positions of receivers, the azimuthal angle ranges from  $0^\circ$  to  $348.75^\circ$  with the step of  $11.25^\circ$ , and the polar angle ranges from  $30^\circ$  to  $150^\circ$  with the step of  $30^\circ$ . The schematic diagram of the locations of the transmitters and receivers around the region of interest is shown in Fig. 8. The entire 3D MNIST dataset is used, including 5k images for training purposes and 1k images for testing.

## B.2 Metrics

Following previous work [21], we evaluate the quantitative performance of our method using PSNR [37], SSIM [38], and Relative Root-Mean-Square Error (MSE) [34]. For PSNR and SSIM, a higher value indicates better performance. For MSE, a lower value indicates better performance. MSE is a metric widely used in EISP, which is defined as follows:

$$\text{MSE} = \left( \frac{1}{M \times M} \sum_{m=1}^M \sum_{n=1}^M \left| \frac{\hat{\epsilon}_r(m, n) - \epsilon_r(m, n)}{\epsilon_r(m, n)} \right|^2 \right)^{\frac{1}{2}}, \quad (12)$$

where  $\epsilon_r(m, n)$  and  $\hat{\epsilon}_r(m, n)$  are the GT and predicted discrete relative permittivity of the unknown scatterers at location  $(m, n)$ , respectively, and  $M \times M$  is the total number of subunits over the Region of Interest (ROI)  $\mathcal{D}$ .

## B.3 Implementation Details

We implement our method using PyTorch. Our MLP consists of 8 layers, each with 256 channels. ReLU activation is used between layers to ensure nonlinear expressiveness. Apply positional encoding to  $\mathbf{x}$  before inputting it into MLP. Use tanh activation in the output layer to improve the stability and convergence of training.

During training, we discretize the region of interest  $\mathcal{D}$  into a  $64 \times 64$  grid and optimize the model using the Adam optimizer with default values  $\beta_1 = 0.9$ ,  $\beta_2 = 0.999$ ,  $\epsilon = 10^{-8}$ , and an initial learning rate of  $1 \times 10^{-3}$ , which decays via a StepLR scheduler (step\_size=10,  $\gamma = 0.8$ ). We set the hyperparameters for the total loss as  $\lambda_{curr} = 100$ ,  $\lambda_{perm} = 10^{-3}$ ,  $\lambda_{scat} = 10^{-7}$ . These weights are chosen to balance the different scales of each loss term, ensuring comparable contributions during



optimization. To prevent exploding gradients, we apply gradient clipping with a maximum norm of  $10^{-4}$ . Positional encoding uses frequency  $\Omega = 10$ , and training runs for 300 iterations on an NVIDIA V100 GPU.

## C Additional Experimental Results

This section provides additional experimental results, including statistical validation (Appx. C.1) and extended qualitative comparisons (Appx. C.2). The latter includes more visual comparisons with baseline methods, as well as supplementary ablation studies on transmitter robustness and loss design.

### C.1 Experimental Statistical Significance

Given the inherent stochasticity of the additive noise in our experiments, all quantitative results reported in the main manuscript represent averages over 3 independent trials. The noise samples were independently drawn from a  $\mathcal{N}(0, 1)$  distribution and subsequently scaled according to both the signal amplitude and the predefined noise ratios (5% and 30%). We report the mean and standard deviation (std) in Table 5, which shows that the experimental variations introduced less than 1% error, confirming the statistical significance of our results.

Table 5: **Statistical results of quantitative metrics.** For Circular and MNIST datasets, we report the mean and standard deviation (std) over 3 independent trials under two noise levels: 5% and 30%.

	MNIST (5%)			MNIST (30%)			Circular (5%)			Circular (30%)		
	MSE ↓	SSIM ↑	PSNR ↑	MSE ↓	SSIM ↑	PSNR ↑	MSE ↓	SSIM ↑	PSNR ↑	MSE ↓	SSIM ↑	PSNR ↑
Number of Transmitters: $N = 16$												
mean	0.055	0.955	29.31	0.077	0.923	26.52	0.021	0.961	36.74	0.027	0.942	34.23
std	$3.7 \times 10^{-5}$	$2.4 \times 10^{-5}$	$2.6 \times 10^{-3}$	$5.0 \times 10^{-5}$	$1.1 \times 10^{-4}$	$3.2 \times 10^{-3}$	$9.0 \times 10^{-6}$	$2.6 \times 10^{-5}$	$1.5 \times 10^{-3}$	$2.1 \times 10^{-5}$	$2.1 \times 10^{-5}$	$3.4 \times 10^{-3}$
Number of Transmitters: $N = 1$												
mean	0.079	0.914	26.41	0.111	0.864	23.56	0.028	0.941	34.16	0.037	0.916	31.93
std	$2.8 \times 10^{-5}$	$4.9 \times 10^{-5}$	$1.8 \times 10^{-3}$	$1.2 \times 10^{-4}$	$2.0 \times 10^{-4}$	$7.9 \times 10^{-3}$	$8.0 \times 10^{-6}$	$8.0 \times 10^{-6}$	$2.7 \times 10^{-3}$	$7.0 \times 10^{-6}$	$6.1 \times 10^{-5}$	$6.6 \times 10^{-3}$

### C.2 Additional Qualitative Results

**Qualitative Comparison.** We present more qualitative comparison on Circular dataset [22] and MNIST dataset [9] under settings with different transmitter numbers  $N$  and noise levels, as shown in Fig. 9 to Fig. 14. We also present qualitative comparison on IF [12] dataset under the single-transmitter setting, as shown in Fig. 15. Our method achieves comparable or superior performance to SOTA methods in most cases under multiple-transmitter settings, as Fig. 9, Fig. 10, Fig. 13, and Fig. 14 indicate. As shown in Fig. 10 and Fig. 14, PGAN [34] introduces noticeable background artifacts due to the lack of consideration of physics. And Fig. 9 shows that Img-Interiors occasionally fails to converge due to local optima.

For single-transmitter setting ( $N = 1$ ), our method significantly outperforms all previous approaches across all datasets, as shown in Fig. 11 and Fig. 12. Conventional methods such as BP[2], Gs SOM [4], and 2-fold SOM [4] produce only blurry reconstructions. Deep learning-based methods such as BPS [5], Physics-Net [21], and PGAN [34] tend to “hallucinate” the digit, leading to wrong reconstruction on the MNIST dataset. Img-Interiors [22] suffers from degeneration and can only produce spherical wave patterns. In contrast, our method can still produce reasonably accurate reconstructions of the relative permittivity under such a challenging condition. This enables practical applications with fewer transmitters, significantly reducing deployment costs while preserving reconstruction quality.

**3D Reconstruction.** We present more qualitative comparison on 3D MNIST dataset under the single-transmitter setting, as shown in Fig. 16. Our method successfully approximates permittivity reconstruction even in this difficult setting, whereas Img-Interiors [22] fails. Similar to the 2D scenario, Img-Interiors suffers from degeneration and can only produce fixed patterns, failing to capture the shape of scatterers.

**Transmitter Robustness.** We present qualitative results under varying transmitter numbers  $N$  on the MNIST dataset at a 5% noise level, as shown in Fig. 17. As it indicates, our method demonstrates strong robustness under sparse-transmitter setting. For  $N = 8$  and  $N = 4$ , the visual quality degrades

only slightly compared to the full setting with  $N = 16$ . Even for a single-transmitter setting ( $N = 1$ ), our method still successfully produces a basic reconstruction of the scatter outline.

**Loss Ablation.** We present qualitative results of our loss ablations on both the MNIST dataset and IF dataset, as shown in Fig. 18 and Fig. 19. Compared to using (a) only the *current* loss  $\mathcal{L}_{\text{curr}}$ , incorporating (b) the *permittivity* loss  $\mathcal{L}_{\text{perm}}$  significantly enhances visual quality. In contrast, adding the (c) *scattering* loss  $\mathcal{L}_{\text{scat}}$  alone yields limited improvement, likely due to training noise causing deviations from the inverse scattering stage. When all three loss terms are combined (d), our full model achieves the best visual results.

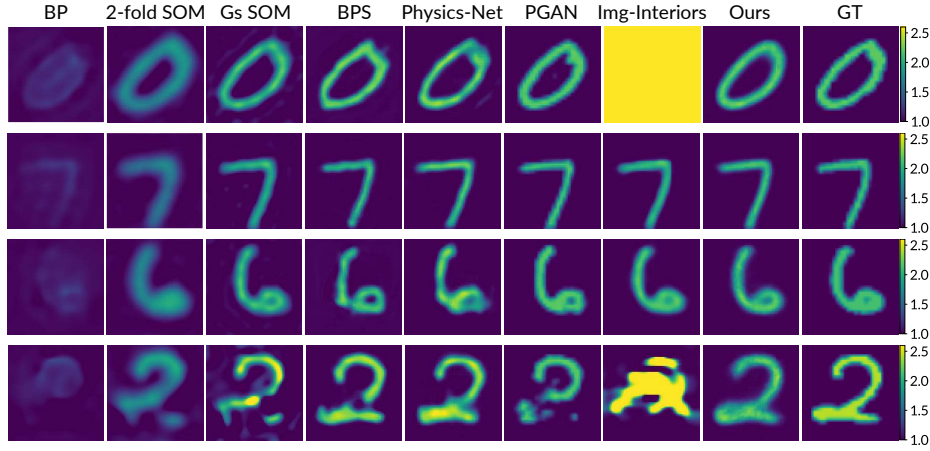


Figure 9: **Qualitative comparison under the multiple-transmitter setting on MNIST dataset.** The results are obtained with  $N = 16$  transmitters and a noise level of 5%. Colors represent the values of the relative permittivity.

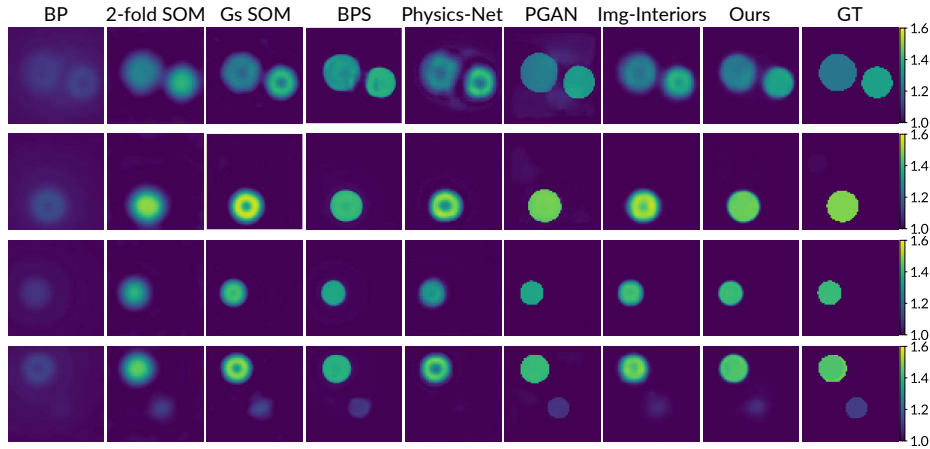


Figure 10: **Qualitative comparison under the multiple-transmitter setting on Circular dataset.** The results are obtained with  $N = 16$  transmitters and a noise level of 5%. Colors represent the values of the relative permittivity.

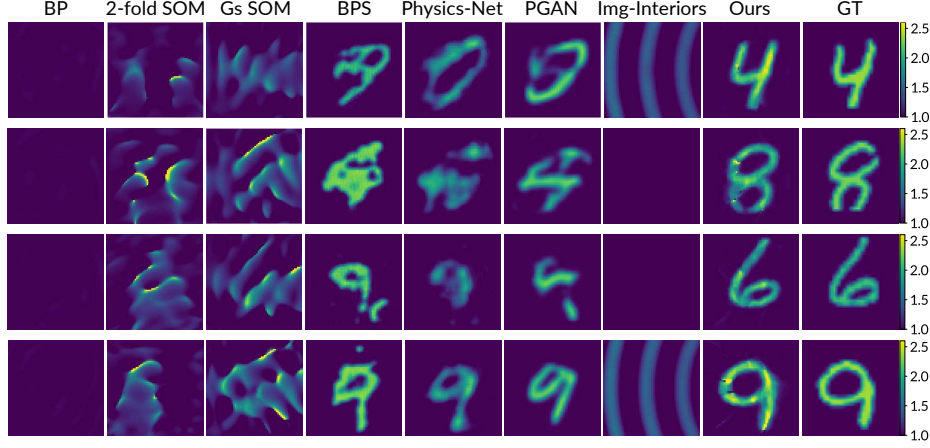


Figure 11: **Qualitative comparison under the single-transmitter setting on MNIST dataset.** The results are obtained with  $N = 1$  transmitter and a noise level of 5%. Colors represent the values of the relative permittivity.

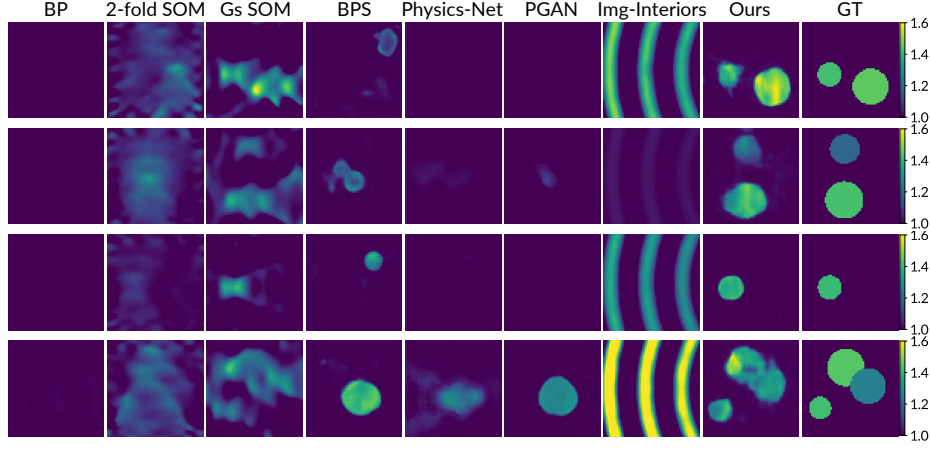


Figure 12: **Qualitative comparison under the single-transmitter setting on Circular dataset.** The results are obtained with  $N = 1$  transmitter and a noise level of 5%. Colors represent the values of the relative permittivity.

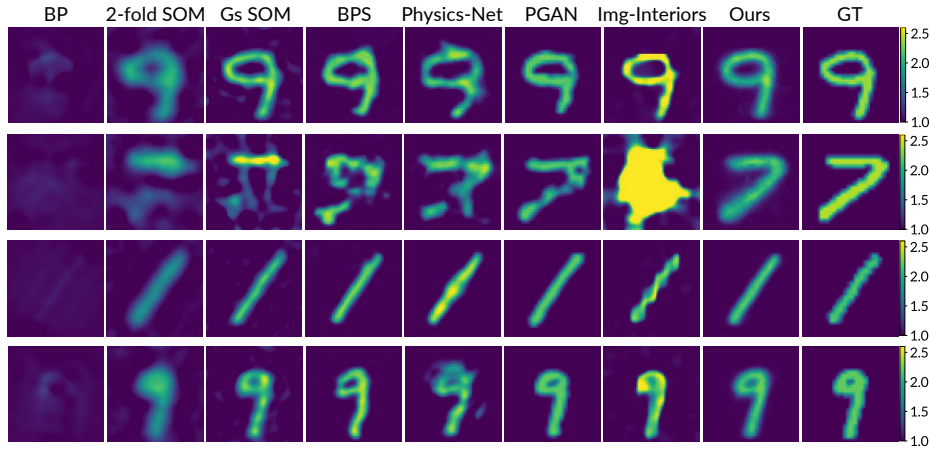


Figure 13: **Qualitative comparison under high noise setting on MNIST dataset.** The results are obtained with  $N = 16$  transmitters and a noise level of 30%. Colors represent the values of the relative permittivity.

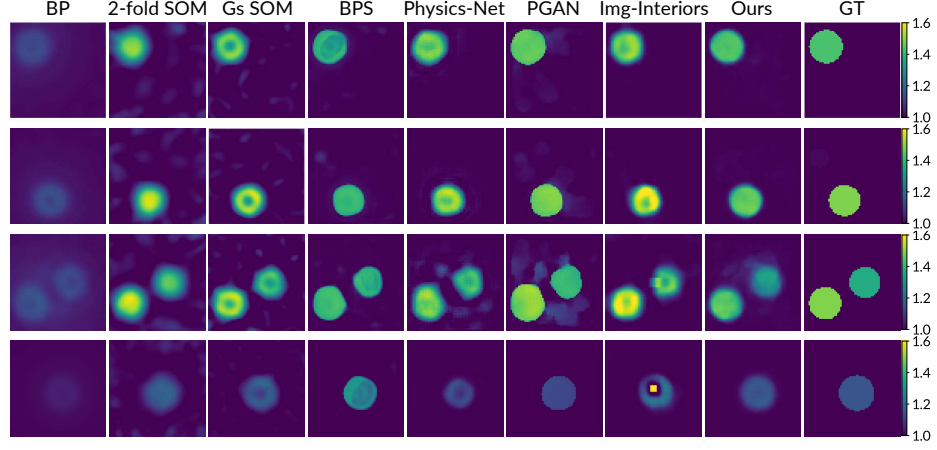


Figure 14: **Qualitative comparison under high noise setting on Circular dataset.** The results are obtained with  $N = 16$  transmitters and a noise level of 30%. Colors represent the values of the relative permittivity.

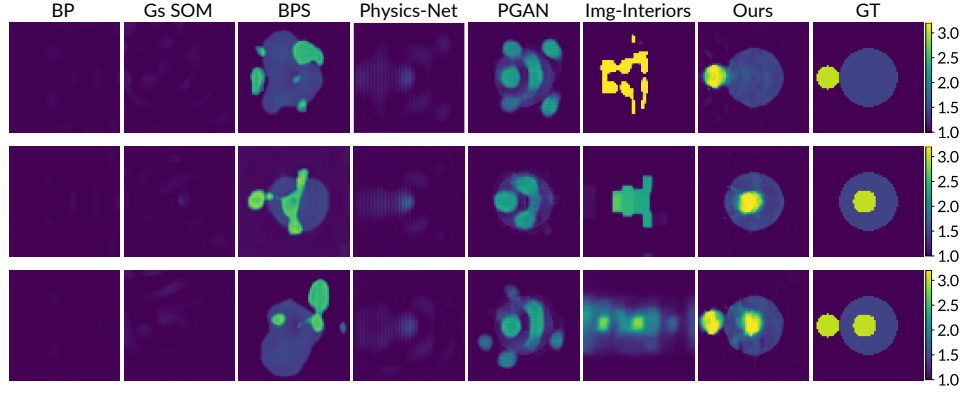


Figure 15: **Qualitative comparison under single-transmitter setting on IF dataset.** The results are obtained with  $N = 1$  transmitter, without noise level. Colors represent the values of the relative permittivity.

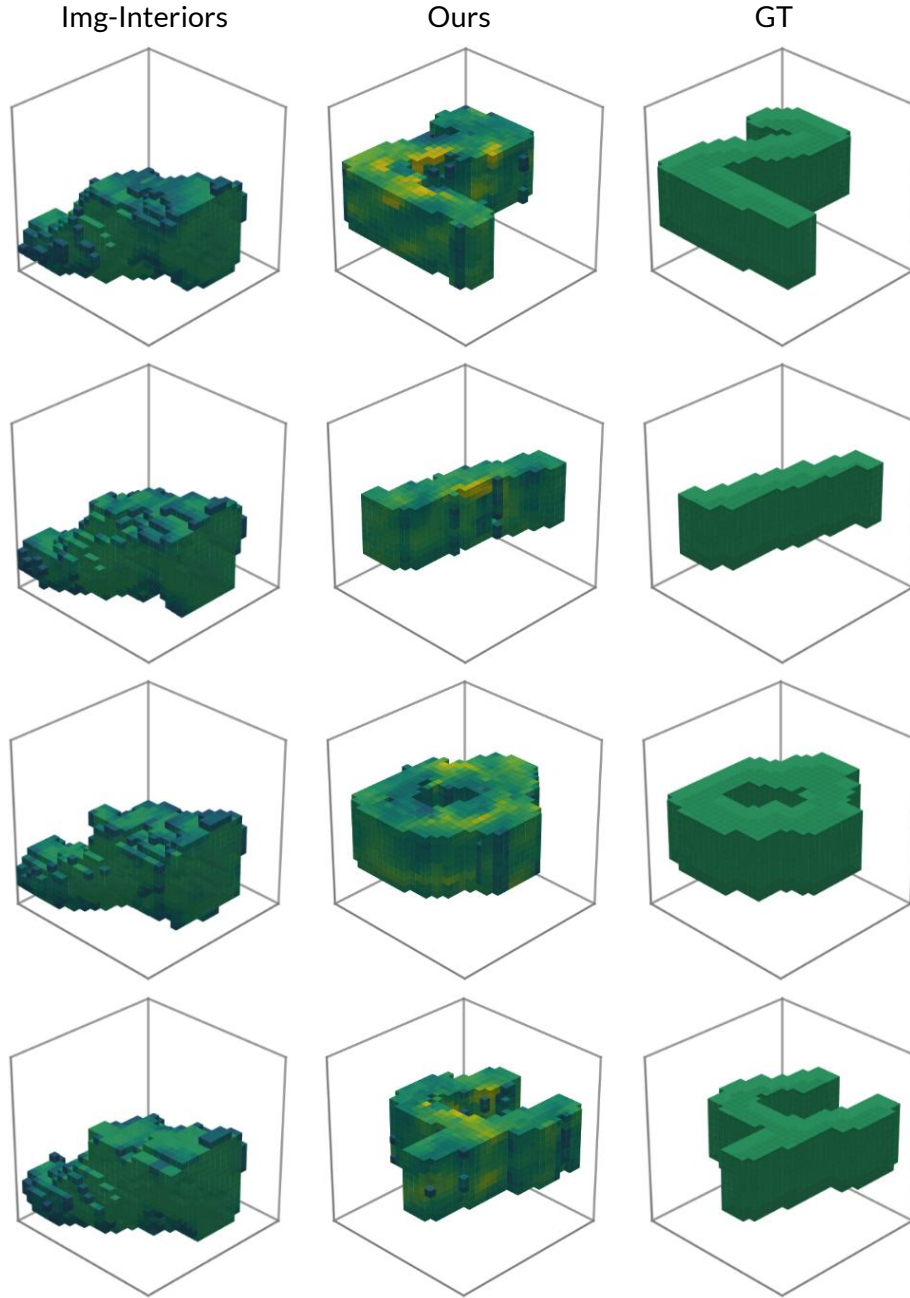


Figure 16: **Qualitative comparison under the single-transmitter setting for 3D reconstruction.** The results are obtained with single transmitter ( $N = 1$ ). The voxel colors represent the values of the relative permittivity.

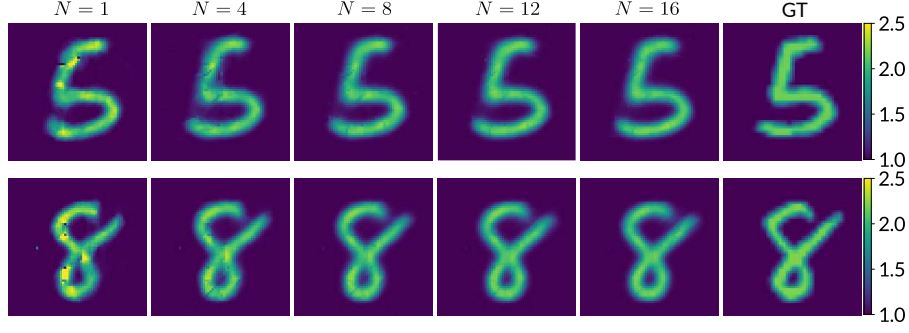


Figure 17: **Qualitative results of our method versus transmitter number on the MNIST dataset under the noise level of 5%.** Colors represent the values of the relative permittivity.

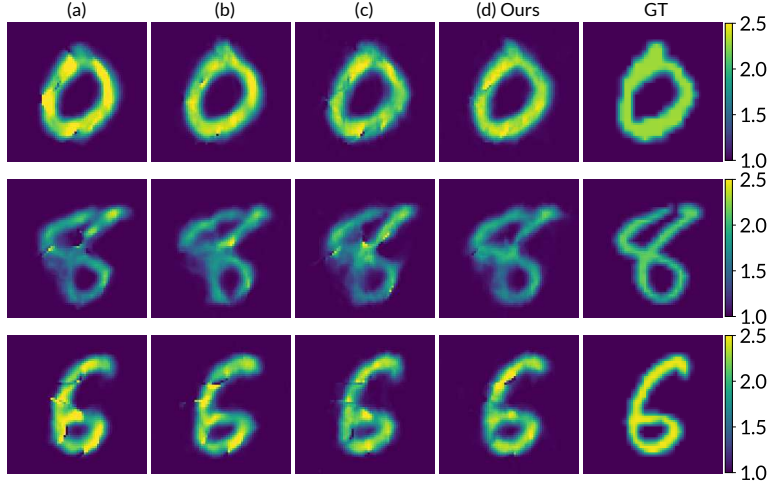


Figure 18: **Qualitative results of our loss ablations on the MNIST dataset.** The results are obtained with  $N = 1$  transmitters and a noise level of 5%. (a)  $\mathcal{L}_{\text{curr}}$  only; (b)  $\mathcal{L}_{\text{curr}} + \mathcal{L}_{\text{perm}}$ ; (c)  $\mathcal{L}_{\text{curr}} + \mathcal{L}_{\text{scat}}$ ; (d) our method with full loss.

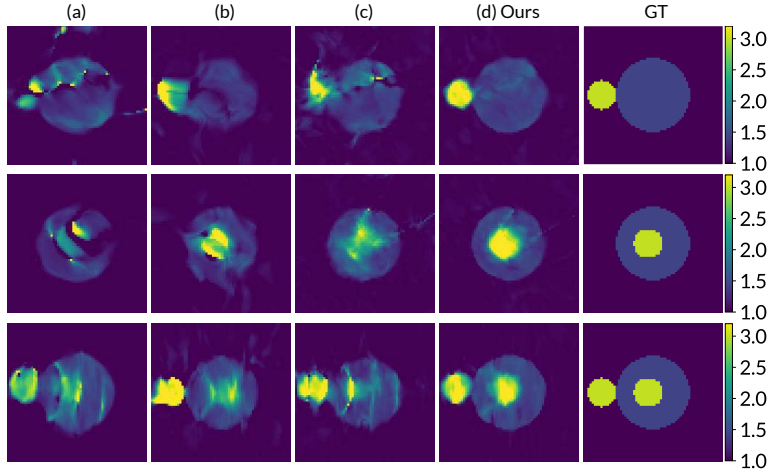


Figure 19: **Qualitative results of our loss ablations on the IF dataset.** The results are obtained with  $N = 1$  transmitters. (a)  $\mathcal{L}_{\text{curr}}$  only; (b)  $\mathcal{L}_{\text{curr}} + \mathcal{L}_{\text{perm}}$ ; (c)  $\mathcal{L}_{\text{curr}} + \mathcal{L}_{\text{scat}}$ ; (d) our method with full loss.